RSC Advances

PAPER

View Article Online
View Journal | View Issue



Cite this: *RSC Adv.*, 2024, **14**, 10776

# Industrial-scale feasibility for textile wastewater treatment *via* Photocatalysis-adsorption technology using black sand and UV lamp†

Rabab Wagdy,[a] Mahmoud F. Mubarak,[b] Rasha S. Mohamed[c] and Abeer El Shahawy *[d]

Dye-contaminated wastewater is a major environmental problem that requires effective and affordable treatment methods. This study investigates an innovative approach using black sand filtration assisted by UV light to remove methylene blue (MB) dye from wastewater. The motivation is to develop a sustainable low-cost wastewater treatment technology. Black sand's composition of iron oxide and other metal oxides enables the adsorption and photocatalytic degradation of dyes. The effects of operating parameters, including pH, bed height, flow rate, and initial MB concentration, were examined using a fixed-bed column system. The maximum adsorption capacity was 562.43 mg $g^{-1}$ at optimal pH 10, 15 cm bed height, 50 ppm MB, and 53.33 mL $min^{-1}$ flow rate. Mathematical models effectively described the experimental breakthrough curves. For real textile wastewater, black sand with a UV lamp removed 50.40% COD, 73.68% TDS, 43.82% TSS, and 98.57% conductivity, significantly outperforming filtration without UV assistance. Characterization *via* XRD, XRF, FTIR, zeta potential, and SEM revealed black sand's photocatalytic properties and mechanism of MB adsorption. The findings demonstrate black sand filtration plus UV irradiation as a feasible, sustainable technology for removing dyes and organics from wastewater. This method has promise for the scale-up treatment of textiles and other industrial effluents.

Received 16th January 2024
Accepted 14th March 2024

DOI: 10.1039/d4ra00421c

rsc.li/rsc-advances



## Introduction

Growing industrialization and water pollution have created an urgent need for effective and affordable wastewater treatment technologies. Conventional methods such as coagulation, activated sludge, and electrolysis have drawbacks, including high costs and process complexities. Adsorption is advantageous due to its efficiency, versatility, and environmentally friendly nature; however, activated carbon adsorbents remain expensive.[1–4]

Recent research has focused on developing low-cost high-performance adsorbents from agricultural and mineral sources. Various studies have used iron oxide-rich sands for dye removal but primarily in batch experiments, which do not translate directly to large-scale column performance. Photocatalysis also shows promise for degrading recalcitrant dyes with metal oxide photocatalysts such as $TiO_2$ and ZnO demonstrating effectiveness.[3–5]

This study investigates an innovative combined adsorption-photocatalytic method that uses inexpensive and abundant black sand, assisted by UV irradiation, to remove methylene blue (MB) dye from water. The motivation is to develop a sustainable low-cost wastewater treatment alternative to activated carbon for organic contaminant removal.[6–12]

This work uniquely integrates adsorptive filtration using locally available black sand with photocatalytic degradation enabled by UV irradiation to remove dyes from wastewater. The novelty lies in using inexpensive black sand containing iron, titanium, and other metal oxides to enable a synergistic combination of adsorption capacity and UV-activated photocatalysis.

Although prior studies have independently explored black sand for filtration or photocatalysis, this integrated approach advances dye removal performance. The continuous fixed-bed column experiments provide practical insights unattainable from batch studies, demonstrating up to 90% dye removal and 562 mg $g^{-1}$ maximum adsorption capacity under optimized conditions.

This first investigation confirms effective dye removal from real textile wastewaters, with 73% TDS, 50% COD, and 99% conductivity reductions. Comparable works utilizing waste-

[a]*Environmental Engineering Department, Faculty of Engineering, Zagazig University, Postal code 44519, Zagazig, Egypt. E-mail: Rabab_wagdy@yahoo.com*

[b]*Petroleum Applications Department, Egyptian Petroleum Research Institute (EPRI), Nasr City, Cairo 11727, Egypt. E-mail: Fathy8753@yahoo.com; Fathy8753@epri.sci.eg*

[c]*Refining Division, Egyptian Petroleum Research Institute, 1 Ahmed El-Zomor St., Nasr City, 11727, Cairo, Egypt. E-mail: rashaepri2009@yahoo.com*

[d]*Department of Civil Engineering, Faculty of Engineering, Suez Canal University, Environmental Engineering, P.O. Box 41522, Ismailia, Egypt. E-mail: abeer_shahawi@eng.suez.edu.eg*

† Electronic supplementary information (ESI) available. See DOI: https://doi.org/10.1039/d4ra00421c

derived adsorbents have reported lower treatment efficiencies despite higher operating costs.

This work delivers a sustainable, scalable, and affordable wastewater treatment alternative by leveraging locally available materials through an innovative configuration. The combined adsorption-photocatalysis system enabled by black sand and UV assistance demonstrates efficiency, economy, and eco-friendliness advancements over existing solutions.

This work uniquely utilizes black sand's iron oxide composition to enable dye adsorption, together with UV light, to activate photocatalytic degradation. It advances beyond batch studies to systematically examine treatment performance in a continuous fixed-bed column across variations in operating parameters. The combined adsorption-photocatalytic mechanism could enable scalable, affordable organic removal from industrial effluents.

## Materials and methods

### Materials

Natural sand was harvested at the Rasheed facility at Abu-Khashaba Beach.[13] Synthetic water was changed using NaOH (0.1 M) or HCl (0.1 M) for the desired pH. All chemicals used were of analytical quality and were obtained from Egypt. Methylene blue (MB) was supplied by HiMedia Laboratories Pvt. Ltd. The chemical structure of methylene blue (MB) dye is shown in Fig. 1.[5] Industrial effluent from the Emessa Denim factory in Beni-Suef, Egypt, was used as a wastewater model. The cationic nature due to positively charged nitrogen atoms enables electrostatic interactions with the negatively charged surface of the black sand photocatalyst. Polyethylene bottles with a 10 L capacity held all the samples. Before and after black sand filtration, pH, conductivity, TSS, TDS, and chemical oxygen demand (COD) experiments are carried out.

### Characterization techniques

**Instrumentation.** An X-ray fluorescence (XRF) analysis was carried out on the elemental composition of the black sand using a Panalytical AXIOS PW4400 spectrophotometer. A 50 kV accelerating voltage was applied to the radiation source's Rh tube. The X'Pert PRO PANalytical system is a commonly used X-ray diffraction instrument. In this case, Cu K± radiation with a wavelength of 0.15406 nm was utilized. The scanning rate, which refers to the speed at which the XRD patterns were recorded, was set at 0.02 $s^{-1}$. The material was examined with a scanning electron microscope (SEM) to see how it works (Hitachi S4800 instrument). The Fourier transform infrared (FTIR) spectrometer examined the molecular structure. A Bruker ALPHA spectrophotometer was used to measure the 4000–400 $cm^{-1}$ spectra. The average aggregate size of the black sand particles was detected using the dynamic light scattering (DLS) particle sizing/zeta potential instrument technique and a zeta sizer nano series HT (Nano-ZS). The sample was mixed with water using sound waves for 15 minutes and then measured in a quartz cuvette. Using a UV-VIS spectrophotometer, the amount of dye in the water solution was found (Shimadzu-1601).

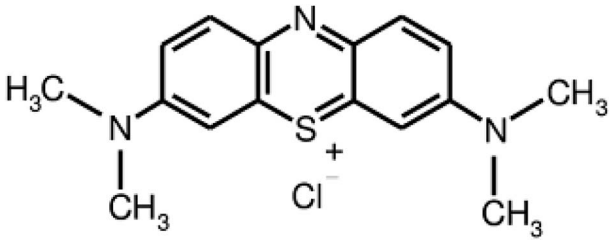


Fig. 1 Chemical structure of methylene blue (MB) dye.

### Pilot scale description

The adsorption studies are carried out utilizing a 45 cm-tall plastic column with an interior dimension of 8 cm, as shown in Fig. 2. In the column, 2750 g of black sand was sandwiched between the glass wool at all times. This was done to avoid the black sand's wash-out and ensure appropriate liquid distribution. This is why the upper and lower ends of the column have a perforated plate that allows the treated wastewater to flow. This prevents the sand particles from moving. The adsorbent in the column had an average packed density of 2.2 g $cm^{-3}$. UV light has a wavelength of 254 nm, 15 mm in diameter, and 225 mm in length. It is powered by 11 W and comes from Philips TUV in Poland. The UV lamp is at the column centerline, surrounded by polluted water. Downward motion was used for the flow of the dye solution, which had a concentration ($C_o$) ranging from 50 to 350 ppm. The effluent samples were taken at regular intervals (0.5–10 h) with a volume of 700 mL, and a UV-Vis spectrophotometer was used to assess the samples and the residual dye content ($C_t$). The research used bed heights of 8, 15, and 25 cm, and flow rates ranging from 53.33 to 210 mL $min^{-1}$.

Considering the effluent breakthrough curves while designing the adsorption column is crucial. The dynamic adsorption column at work has been predicted using various kinetic models, including the Yoon–Nelson, Bohart–Adams, and Thomas models.[6]

A multimeter called ASWA AD 1030 pH $mV^{-1}$ was used to measure the pH. The CONS800 C864 multiparameter was used to measure conductivity. All the measurements have been performed according to the rules set by (APHA, 2017).[14]

### Column study modeling

One could model the data accumulated from column experiments to evaluate the possibility of scaling up. Plotting the effluent solute concentration over time yields an important curve that can be used to characterize the dynamic behaviour of a packed column. A breakthrough point is the point at which the allowed solute concentration in the effluent is reached. The experimental breakthrough curves were fitted to the Thomas, Yoon–Nelson, and Adams–Bohart models using non-linear regression analysis. The Thomas model provided the best correlation, with an $R^2$ value of 0.98, indicating that it most accurately described the adsorption dynamics in the fixed-bed column under test conditions.[5,15]

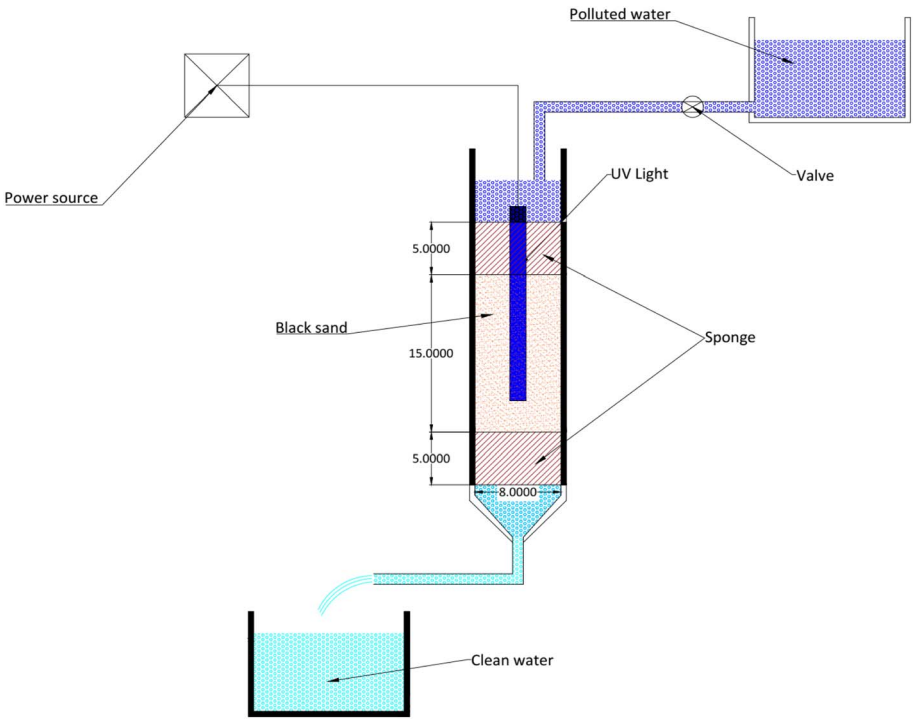


Fig. 2 Schematic diagram of the pilot-scale filter system.

### Data analysis

Specifically, one-factor ANOVA was used to analyze the results of the pH effect experiments to determine if the differences in MB removal were statistically significant between pH values.

### Experimental plan

A factorial design was implemented to evaluate the effects of four key operating parameters on the black sand filtration system's methylene blue (MB) removal efficiency: pH, bed height, flow rate, and contact time. Each parameter was tested at three levels, as summarized below: pH: 4, 7, and 10; bed height: 10 cm, 15 cm, and 20 cm; flow rate: 100 mL $min^{-1}$, 200 mL $min^{-1}$, and 300 mL $min^{-1}$; and contact time: 2 hours, 6 hours, and 10 hours; MB concentration was fixed at 100 ppm for all the tests. A total of 81 experimental trials were performed to cover all possible parameter combinations. The inlet and outlet MB concentrations were analyzed to determine the removal efficiency.

## Results and discussions

### X-ray fluorescence (XRF) of black sand

According to Table 1, the fluorescence spectroscopy X-ray (XRF) analysis results of the chromatically sorted samples show how the masses were distributed and the chemicals in each fraction. In XRF analysis, it is essential to note that the oxides observed may be parts of other compounds, as shown by earlier tests, such as XRD, FTIR, and others. Quartz sand contains various chemicals, some of which are listed in Table 1: $SiO_2$, CaO, $Fe_2O_3$, and others. Although $Fe_2O_3$ (2.98%) was responsible for the colour of the sand grains, the component $SiO_2$ had the highest proportion at 84.4%.[16] The black sand exhibits a wide range of $Al_2O_3$ (3.4 wt%), CaO (3%), and $TiO_2$ (1.88%), with the lowest percentages of MgO (0.913%), $K_2O$ (0.64%), $Na_2O$ (0.29%), MnO (0.107%) and $P_2O_5$ (0.135%).[17] Results have demonstrated that the samples under investigation include trace amounts of other elements, such as zirconium (Zr), sulfur (S), chlorine (Cl), strontium (Sr), and chromium (Cr).[18] The iron, titanium, and silicon oxides are responsible for the adsorption and photocatalysis mechanisms that enable dye removal rather than just presenting the raw analytical data. This connects the composition results back to the functional properties of interest. The elemental composition determined by XRF

Table 1 XRF analysis of the elemental composition of black sand

| Chemical composition | Main mineral constituents (mass%) |
|---|---|
| $SiO_2$ | 84.4 |
| $Al_2O_3$ | 3.45 |
| $Fe_2O_3$ | 2.98 |
| CaO | 3.00 |
| MgO | 0.913 |
| $K_2O$ | 0.641 |
| $TiO_2$ | 1.88 |
| $Na_2O$ | 0.292 |
| $P_2O_5$ | 0.135 |
| MnO | 0.107 |
| Cr | 0.0359 |
| S | 0.0302 |
| Cl | 0.0570 |
| Sr | 0.0176 |
| Zr | 0.0773 |
| LOI flax | 2.00 |

analysis in this work is comparable to black sand from other regions, as reported by ref. 8 and 9, also showing high $SiO_2$ and iron oxide content. The presence of iron oxides gives black colouration.

### FTIR of black sand

The functional groups of the black sand were studied by FTIR spectra in the range of 400–4000 $cm^{-1}$ (Fig. 3). The functional groups of the black sand were studied by FTIR spectra in the range of 400–4000 $cm^{-1}$ (Fig. 3). FTIR peaks, which indicate metal oxide bonds and surface functional groups, are involved in MB adsorption. The primary characteristics of the IR spectrum of the black sand sample are the weak and strong bands within the 1660–500 $cm^{-1}$ range. Additionally, low-intensity bands at 2385, 2045, and 1828 $cm^{-1}$ are believed to be caused by the organic component (C–H bending) attached to the black sand surface. The single broadband referred to as silanol OH groups shows absorption in the range 950–810 $cm^{-1}$ referred to as silanol OH groups from adsorbed water (H–O–H).[19] At 1135 and 1167 $cm^{-1}$. This can be attributed to Si–O–M asymmetrical stretching vibrations due to low Al or Fe substituted in the silicate mineral lattice. The characteristic feature of black sand is that peaks appear at 740 $cm^{-1}$ and 781 $cm^{-1}$ due to Si–O symmetrical stretching vibration.[20] Moreover, peaks at wavelength 610 $cm^{-1}$ are related to symmetrical bending Si–O vibration, and 699 $cm^{-1}$ are related to O–Si–O, indicating quartz silica existence in crystalline form, and the peak at 554 $cm^{-1}$ attributed to Si–O–Al. The FTIR spectrum of the black sand is consistent with previous studies on similar geological sands,[21] showing signature peaks that indicate the presence of silicate and iron oxide phases.

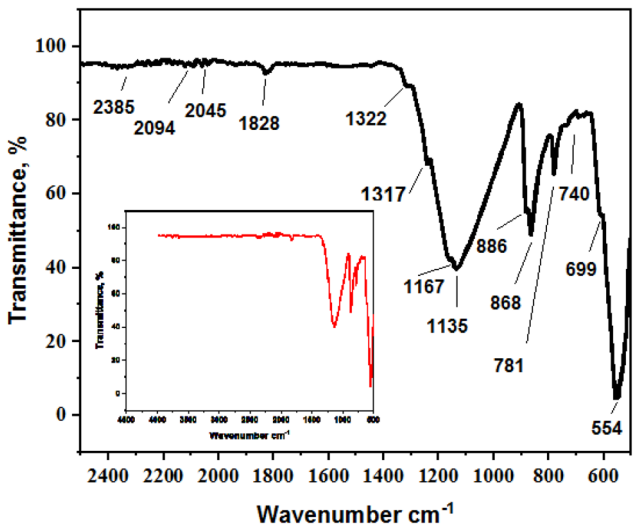


Fig. 3 FTIR spectra of black sand.

### X-ray diffraction

The XRD patterns of the black sand are shown in Fig. 4. Distinct diffraction peaks were observed at 2$\theta$ values of 20.89°, 26.64, 30.12°, 35.48°, 45.84°, and 56.25°, which match well with the reference pattern for quartz $SiO_2$ (JCPDS card #99-0088). Additional peaks were observed at 2$\theta$ values of 18.34°, 27.00°, 28.55°, 30.12°, 35.48°, 37.08° and 43.09°, consistent with hematite $Fe_2O_3$ (JCPDS card #89-0599). Other mineral phases, such as aluminium oxide $Al_2O_3$ (JCPDS #10-0173) with peaks at 32.47° and 62°; calcite $CaCO_3$ (JCPDS #82-1690) with peaks at 28.3°, 31°, 38.1° and 54.5°; and feldspar (JCPDS #87-0653) with a peak at 60°; were also identified. The detected crystalline phases of quartz, iron oxide, aluminium oxide, calcite, and feldspar agree with standard patterns. These phases play an important role in the photocatalytic activity of black sand in removing methylene blue dye under UV light irradiation.[17] Quartz and metal oxides, such as $Fe_2O_3$ and $TiO_2$, can generate electron–hole pairs upon UV excitation, facilitating oxidative degradation of the adsorbed dye *via* radical formation.[10] Although distinct $TiO_2$ peaks were

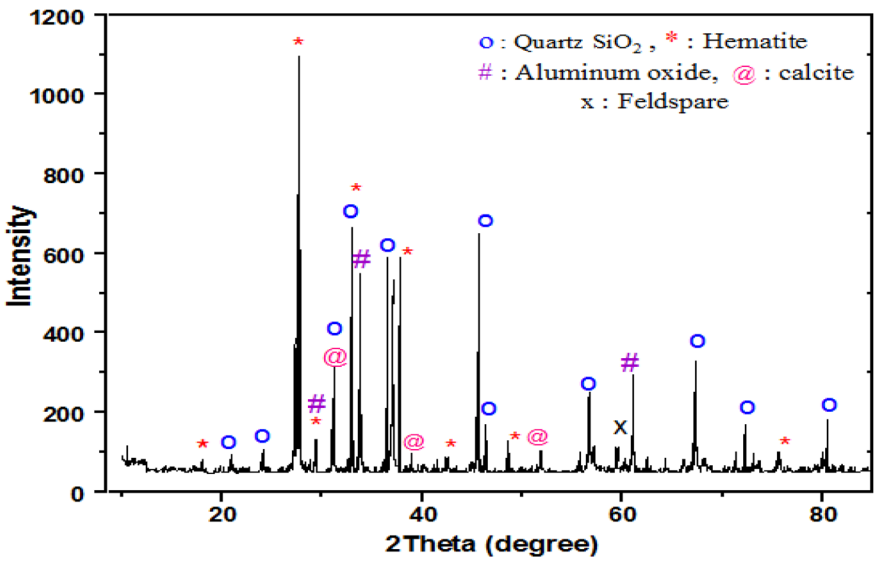


Fig. 4 Representative XRD pattern of the black sand sample.

not observed likely due to titanium incorporation into iron oxide lattices, its presence was still confirmed *via* XRF analysis and contributed to the photocatalytic performance.[22] In summary, XRD analysis validated the mineralogical composition of the black sand and linked it to the proposed dual adsorption-photocatalytic mechanism for effective dye removal.

### SEM analysis of black sand

The SEM analysis aimed to examine the surface morphology and porosity of the black sand particles. However, as evident in Fig. 5a–c, there is little observable difference in morphology or porosity at the magnifications shown. Zoomed-in micrographs showing porous surface morphology and nanoscale texture provide a large surface area for adsorption. Specifically, all images depict the black sand grains as coarse, asymmetric particles with irregular shapes. Although the SEM enables the characterization of surface properties, it does not identify changes to the sand particles with the adsorption of methylene blue dye in this study. This could be due to limitations in the magnification scale, where dye molecule deposition on the particle surfaces is below the detection threshold.

The authors compare SEM findings with relevant literature reports to elucidate the adsorption mechanisms better and confirm dye binding. The particle size and morphology observed in the SEM imaging are comparable to black sands from the Nile region, as analyzed by ref. 8 and 9, showing predominantly coarse irregular grains. Ansari *et al.* demonstrated successful SEM imaging of methylene blue adsorbed onto cauliflower leaves, appearing as distinct dark spots across the particle surface.[23] Such corroborative analysis is currently lacking and would strengthen the evidence for dye adsorption onto the black sand.

Attractive van der Waals forces cause black sand aggregation in the samples to spread out in the water. The dispersing conditions can be changed to eliminate these aggregates by adding repulsive forces between the particles.[24] The particle size of the black sand sample was 27.8 mm, and the zeta potential was −25.3 mV, as illustrated in Table 2.

### Correlating characterization results

The combination of XRD, XRF, FTIR, SEM, and zeta potential characterization offers comprehensive insights into the composition, morphology, surface chemistry, and properties of the black sand media responsible for enabling methylene blue (MB) dye adsorption and photocatalytic degradation.

The prominence of elemental silicon, iron, aluminium, calcium, and titanium oxides revealed in the XRF analysis correlates with the crystalline phases of $SiO_2$, $Fe_2O_3$, $Al_2O_3$, CaO, and $TiO_2$ identified by XRD patterns. The metal oxides confer surface charges for electrostatic interactions with cationic MB molecules, as confirmed by the negative zeta potential value. FTIR spectra indicate hydroxyl, carboxyl, carbonyl, and aromatic groups on the heterogeneous sand particles as potential active binding sites interacting with MB dye. This aligns with the irregular, porous morphology revealed in the SEM micrographs, which visualize the surface area available for adsorption. The spectroscopic signatures of the metal oxide functional groups in the sand additionally explain the photocatalytic mechanism initiated upon UV irradiation. As the bandgap excitation of $TiO_2$ and iron oxide generates electron–hole pairs, oxidative degradation of the adsorbed dye occurs through radical formation. The complementary analytical techniques characterize the adsorptive and photocatalytic properties of the black sand media, synergistically enabling efficient dye removal from wastewater. The results mutually reinforce the integrated adsorption-photocatalysis system's proposed dual mechanism of MB dye elimination.

### Column adsorption parameters

**Effect of pH on black sand assisted with and without UV lamp.** The pH influences methylene blue (MB) removal due to its impact on the surface charge of the adsorbent and the dye molecule speciation in solution. As reported by Halim *et al.*, cationic dyes exhibit enhanced adsorption under alkaline conditions due to favourable electrostatic interactions with the negatively charged adsorbent surface.[15] Although pH 8–10 was found to be optimal for MB removal by the black sand (Fig. S1, ESI†), removal efficiency generally decreased above pH 10 due to the excessive deprotonation of surface sites at pH 12, reducing the affinity for the positively charged dye molecules, where deprotonation of surface hydroxyl groups likely imparts a net negative charge. Excess $H^+$ ions compete with and hinder cationic dye adsorption at very low pH.[6] This is because $H^+$ ions compete with the cation dye during adsorption, making the removal of methylene blue from pH 8 to 10 6 easier.

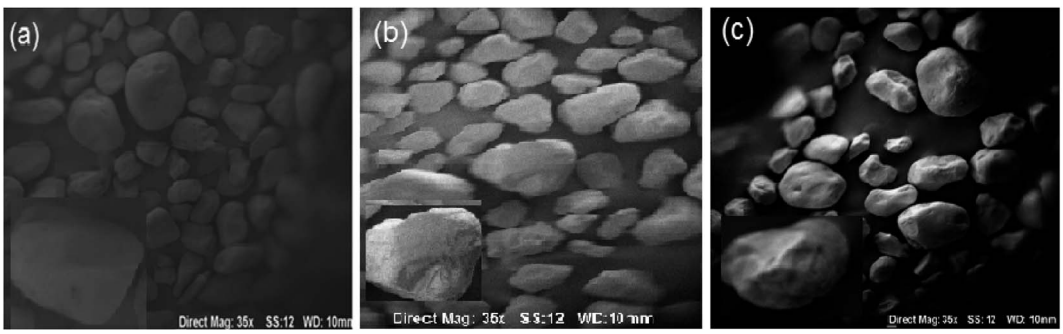


Fig. 5 SEM of black sand sample (a), sand with MB on top of column (b), and sand with MB on bottom of column (c).

 

Table 2 Average aggregate size of the black sample

| Materials | Black sand |
|---|---|
| Average aggregate size (mm) | 27.8 |
| Zeta potential (mV) | −25.3 |

**Black sand depth effect on black sand assisted with and without UV lamp.** However, Fig. S2 (refer to ESI†) clearly shows that the removal ratios achieved with UV assistance were consistently and significantly higher than those without UV across all bed heights tested. This confirms the positive synergistic effect of combining adsorption with UV photocatalysis for dye removal, increasing the depth of black sand and increasing the removal ratio percentage. In all cases, the removal ratio with depth UV was higher than that without UV. Increasing bed height from 10 cm to 20 cm improved MB removal by providing greater surface area and binding sites for adsorption (Kebir *et al.*, 2023).[11] The longer transfer zone also increased the contact time for organic contaminant degradation by reactive radical species. Although pH 10 showed slightly higher removal efficiency than pH 7 in batch testing, the zeta potential results (−25.3 mV at pH 7) indicated that the surface charge was already strongly negative at pH 7. Thus, pH 7 was selected for column tests to avoid unnecessary pH adjustment, which added to process costs without significant gains in performance based on the relatively small difference in removal between pH 7 and 10. A breakthrough curve was observed to become steeper as the bed height increased. The increased amount of black sand, which supplied more functional sites for MB, was responsible for increased breakthrough and exhaustion durations in adsorption due to increased bed depth.[11]

**Flowrate effect on black sand at two MB conc. assisted with UV lamp.** Another experiment was studied to illustrate the effect of flow rate on the removal ratio at pH 10 and 15 cm sand height with and without UV, as illustrated in Fig. S3 (refer to ESI†); it is shown that increasing flow rate decreases the removal ratio. The highest removal ratio was at 50 ppm at 0.053 L $min^{-1}$ with UV; this value was 90%, gradually reducing to 79% at 0.21 L $min^{-1}$ at the same ppm and the same sand height with UV. High concentrations of $C_o$ caused the adsorption sites to run out quickly, which shortened the breakthrough and exhaustion times.

Although there was mass transfer resistance between the adsorbent and the solution, higher influent dye concentrations ($C_o$) drove the adsorption process more strongly, leading to initially better column performance. However, at lower $C_o$ concentrations, the breakthrough curves became more gradual as the adsorption sites were saturated more slowly.[11] This meant that sorption sites ran out faster, and MB uptake was less effective when the concentrations were high. They quickly reached a breaking point, and at low flow rates, the adsorption worked better. Consequently, fewer MB ions were on the bed column because they did not have enough time to live there. This was because the solute could not move quickly through the adsorbent pores.[11] Higher flow rates showed a shorter mass transfer zone, but low flow rates had the highest MB removal percentage uptake (53.33 mL $min^{-1}$).

**Contact time effect on black sand assisted with and without UV lamp.** The effect of contact duration on the removal ratio with and without UV is depicted in Fig. S4 (refer to ESI†). It is shown that at 10 h contact time, the removal ratio was the lowest without UV assistance, achieving only 39% removal. This decrease in performance at the longest contact time of 10 hours can be attributed to the saturation of adsorption sites on the black sand particles. Once saturation was reached, additional contact time did not further increase dye removal. In contrast, at the shortest contact time of 0.5 hours, the removal ratio was higher at 64.5% without UV, indicating that the adsorption sites had not been fully saturated. Prolonged contact time favours higher MB adsorption up to the saturation of available binding sites (Halim *et al.* 2015).[15] The observed trend of increasing dye removal from 0.5 to 6 hours reflects this influence, with gradual equilibrium after ∼6 hours. Thus, 10 hours was the optimal contact time to ensure maximum adsorption capacity.[6]

**Dye conc. effect on black sand assisted with UV lamp.** The relationship between dye concentration and removal ratio at different flow rates was studied, as presented in Fig. S5 (refer to ESI†). Different concentrations were applied from 50 ppm to 350 ppm at different flow rates, so the removal ratio differed from 90% at 50 ppm dye concentration to 72.5% at 350 ppm dye concentration at a flow rate of 0.0533 L $min^{-1}$ with UV. Higher influent MB concentrations yield faster saturation and breakthrough due to the exhaustion of a finite number of surface binding sites (Kebir *et al.*, 2023).[11] Concentrations of up to 350 ppm were examined as representative of industrially contaminated effluents, for which treatment times increased, but removal efficiency was slightly compromised. Overall, the system promised to handle elevated and variable dye contamination loads.

**Flowrate effect on black sand at two MB concs.** The effect of flow rate on black sand performance with UV at min and max flow rates was studied at pH 10 for two MB concentrations, as shown in Fig. S6 (refer to ESI†). The contact time ranged from 0.5 to 10 hours at different flow rates (0.21–0.0533 L $min^{-1}$). This different trend at 0.533 L $min^{-1}$ and 200 ppm MB concentration is likely due to mass transfer limitations arising at the higher flow rate and concentration combination. At elevated flow and dye levels, the residence time within the column was insufficient for adsorption equilibrium to be achieved on all available sites before breakthrough occurred. Low flow rates resulted in greater adsorption efficiency and a quicker attainment of the breakthrough threshold. A low flow rate prolongs the residence time and contact between the influent and adsorbent binding sites, thereby improving MB removal efficiency (Kebir *et al.*, 2023).[11] However, very low flow rates reduce throughput. Considering these factors, an optimum flow rate of 53.33 mL $min^{-1}$ was chosen, achieving 90% MB elimination within 10 hours for 50 ppm initial concentrations at the working bed height,[11] where the 90% MB removal percentage was highest at a low flow rate (53.33 mL $min^{-1}$).

### ANOVA and hypothesis testing

Specifically, one-factor ANOVA was used to analyze the results of the pH effect experiments to determine if the differences in MB removal were statistically significant between pH values with and without the use of a UV lamp at flowrates of 107 mL $min^{-1}$ and MB concentration of 200 ppm, and a one-way analysis of variance (ANOVA) was conducted. The obtained $F$ value of 0.087966 is statistically significant and is lower than the crucial $F$ value of 5.317655. This suggests that no substantial distinction was observed in pH levels between the bed and the absence of the UV lamp; hence, the impact on the adsorption capacity was essentially the same. The adsorption capacity of the bed was mostly unaffected by the presence or absence of a UV lamp, as indicated by the lack of a significant change in sand depth ($F$ 2.090211, $F$ crit 7.708647). The influence of the UV lamp on the bed's adsorption capacity was negligible because there was no significant difference in flow rate change between the two conditions ($F = 2.806566$, $F$ crit $= 5.987378$). The contact time change with and without the UV lamp differed significantly ($F =$ 5.877035; $F$ crit $= 4.9747225$), indicating that the UV lamp affected the adsorption capacity of the bed. The absence of a statistically significant difference in MB concentration change in the presence and absence of a UV lamp ($F = 1.062156$; $F$ threshold $= 5.987378$) indicates that the UV lamp did not impact the bed's adsorption capacity.

Compared to 158 mL $min^{-1}$, 108 mL $min^{-1}$, and 53.30 mL $min^{-1}$, the current rate is 210 mL $min^{-1}$. The $t$-test outcomes indicated $t$ values of −11.57, −7.7432, and −11.566 for the values of 158 mL $min^{-1}$, 53.30 mL $min^{-1}$, and 108 mL $min^{-1}$, respectively, which exceeded the critical value of 2.131817. The 210 mL $min^{-1}$ was compared with 158 mL $min^{-1}$, 108 mL $min^{-1}$, and 53.30 mL $min^{-1}$. $T$-test results showed t-values of −7.7432, −11.566, and −11.87 for 158 mL $min^{-1}$, 53.30 mL $min^{-1}$, and 108 mL $min^{-1}$, respectively, were higher than the critical value of 2.131817. This indicates that a considerable difference in each flowrate affects the adsorption capacity of using black sand when treated with UV when 210 mL $min^{-1}$ is compared to 158 mL $min^{-1}$, 108 mL $min^{-1}$, and 53.30 mL $min^{-1}$. This demonstrates that the flow rate of 53.30 mL $min^{-1}$ was superior to that of 158 mL $min^{-1}$, 108 mL $min^{-1}$, and 210 mL $min^{-1}$ in terms of ion adsorption. These studies demonstrate that a flow rate of 53.30 mL $min^{-1}$ is superior to those used for comparison.

**Breakthrough curve.** Synthetic water has methylene blue conc. 50, 200 ppm and pH = 10 at flow rates of 0.0533 and 0.210 L $min^{-1}$, as shown in Fig. S7 (refer to ESI†). The flow to the column continued until the effluent methylene blue at time $t$ ($C_t$) reached the influent Methylene Blue concentration ($C_o$), *viz.*, $C_o - C_t/C_o \approx 0$. At each of the two flowrates with the two different MB concs, the retained amount of MB in the column (column adsorption capacity in ppm) was calculated graphically by numerically integrating the area under the curve $(C_o - C_t)/C_o$ *vs.* service time (as shown in Fig. S7†)[13,25] using the Excel program. The largest percentage of removal occurred at a 53.33 mL $min^{-1}$ flow rate, with a value of 90%. The flow rates were 0.0533 L $min^{-1}$ and 0.210 L $min^{-1}$, with 90% and 82%, respectively.[26] The breakthrough at 45% was 480 min for 50 and 200 ppm. Increasing the initial MB concentration decreased the breakthrough time. Therefore, less water is treated at breakthrough locations.[3] According to the obtained result, the adsorption capacity of the adsorbent is ≈562.43 ppm $g^{-1}$ (ref. 11) @ $Q = 53.33$ mL $min^{-1}$ for MB conc. 50 ppm. This result shows the feasibility of black sand in wastewater treatment. The capacity of the adsorbent was calculated from the area determined by the term $\left(1 - \frac{C_{out}}{C_f}\right)$ calculated by experimental breakthrough curve, as illustrated in Fig. S7.† The integral $\int_0^{t_{END}} \left(1 - \frac{C_{out}}{C_f}\right) dt$ was calculated by applying the trapeze method.[27]

$$q^* = \frac{C^f Q}{1000 m_s} \int_0^{t_{END}} \left(1 - \frac{C_{out}}{C_f}\right) dt, \quad (1)$$

where $q$ – capacity of the adsorbent (meq $g^{-1}$); $C_{out}$ – concentration of MB in the outlet of the column (meq $L^{-1}$); $C_f$ – feed concentration of MB (meq $L^{-1}$); $Q$ – volumetric flow rate ($cm^3$ $min^{-1}$); $t$ – time (min); and $m_s$ – weight of adsorbent (g).[28]

### Modelling of fixed bed adsorption

**Bohart–Adams model.** The basic mathematical correlation proposed by Bohart and Adams (Bohart & Adams, 1920) can be presented as[29]

$$\ln\left(\frac{C_t}{C_0}\right) = K_{AB} C_0 t - \left(K_{AB} N_0 \left(\frac{Z}{F}\right)\right). \quad (2)$$

The model is well suited to the experimental data of MB adsorption on black sand+ UV with the bed height and feed flow rate ($R^2 = 0.96$), as shown in Fig. S8 and Table S1 (refer to ESI†). According to the Adams–Bohart model, axial dispersion does not affect the dynamic adsorption process.[29]

**Yoon–Nelson model.** The mathematical equation of the Yoon–Nelson model can be written as[29]

$$\ln\left(\frac{C_t}{C_0 - C_t}\right) = K_{YN} t - (\tau K_{YN}). \quad (3)$$

Its validity is restricted to the conditions utilized.[29] Experimental results and Yoon–Nelson model predictions match well with $R^2$ of 0.97 and 0.94 for MB conc. 50 and 200 ppm, respectively at $Q = 53.33$ mL $min^{-1}$, for MB on UV+ black sand. Additionally, $R^2$ was 0.44 and 0.94 for the MB conc. 50 and 200 ppm, respectively, at $Q = 210$ mL $min^{-1}$, as shown in Fig. S9 and Table S2 (refer to ESI†).

**Thomson model.** The Thomas model is given by[3]

$$\ln\left(\frac{C_o}{C_t} - 1\right) = \frac{K_{th} q_F m}{Q} - K_{th} C_f t. \quad (4)$$

This study used the Thomas model to describe column breakthrough curves at various bed heights and flow rates. Eqn (5) can also be expressed as[28]

$$\ln\left(\frac{C_o}{C_t}-1\right)=K'(t-t_1). \quad (5)$$

This study established the breakthrough point at $C_t/C_o$ = 0.05 and the exhaustion point ($C_t/C_o$ approached 1.0), as shown in Fig. S10 and Table S3 (refer to ESI†), when the effluent dye concentration approached the influent dye concentration.

Where $K' = k_{Th}C_o$ and $t_1 = q_F m/(QC_f)$.

$K'$ = modified rate constant of Thomas model (L mg$^{-1}$ h$^{-1}$).

This study described column breakthrough curves at various bed heights and flow rates using the Thomas model (eqn (5)). An extended version of the Thomas model can also be expressed as[3]

$$\ln\left(\frac{C_o}{C_t}-1\right)=b_0+b_1t+b_2t^2+\ldots=\sum_i b_i t^i. \quad (6)$$

## Desorption

In this experiment, desorption and subsequent adsorption cycles were conducted three times to evaluate the regenerative capacity of the black sand. In a desorption experiment, the MB was removed from the black sand using hydrochloric acid, sodium chloride, and sulfuric acid. The results showed that hydrochloric acid had the greatest MB desorption rate.[6] The methylene blue uptake was investigated using black sand, and desorption was studied for the 210 mL min$^{-1}$ flow rate.[26,30] The regeneration of the sand was performed with hydrochloric acid (HCl). Three sets of adsorption and desorption cycles were performed to test how readily the system could be used again, as shown in Fig. S11 (refer to ESI†). The MB stuck to the column was washed off in three-bed pH 12.5 Tris buffer volumes during desorption cycle. Breakthrough took 30 minutes, and exhaustion took 480 minutes for the first cycle, which used a treated bed volume of 700 mL. With a treated bed volume of 700 mL, the threshold time for the second cycle was 33 minutes, and the exhaustion time was 460 minutes. With a 700 mL treated bed volume, the third cycle breakthrough took 35 minutes, and exhaustion took 445 minutes. The breakthrough curves varied slightly across the cycles in the experiments. Single-way ANOVA indicated no change across the three cycles ($p = 0.83$).

## Textile wastewater application

For industrial use, black sand had to be tested using the above column to treat real wastewater. The filtration performance of black sand was tested at room temperature under continuous flow. Before the experiments, about 100 mL of demineralized water was run through the column to eliminate any non-consolidated and ensure no soluble species. The Watson Marlow 505 S Peristaltic Pump set the flow rate at 0.107 L min$^{-1}$.

## pH, TSS, TDS, COD, and conductivity

As shown in Table 3, the pH of industrial wastewater had an average value of 8.6. The pH of the treated water was the same. The influent TSS was 890 ppm, while the effluent TSS was 500 and 750 ppm for black sand filtration assisted with and without a UV lamp, respectively. The influent TDS was 950 ppm, while the effluent TDS was 250 and 700 ppm for black sand filtration assisted with and without a UV lamp, respectively. Black sand assisted with UV light and without UV both significantly reduced the organic load (COD: 50% and 15%, respectively) in treated wastewater according to the results of the physicochemical investigations. Table 3 shows that the industrial wastewater had a 950 μS cm$^{-1}$ conductivity because the sand the authors used for our study had a high concentration of ions.[3] After black sand filtration assisted with a UV lamp, it became 13.6 μS cm$^{-1}$. Simultaneously, it was 30 μS cm$^{-1}$ without a UV lamp. Compared to other soil-based systems, such as wetland or compact filtration systems, our filtration system—based on black sand and aided by a UV lamp—showed more effective and stable results in treating wastewater. Unlike Haouti *et al.*[3] who attributed the pH increase after black sand filtration to alkalinity, pH was steady after filtration.

As explored in this study, the combination of black sand and UV lamp resulted in a notable adsorption capacity ($q_{max}$) of 562.43 mg g$^{-1}$. In comparison,[29] a $q_{max}$ of 412.7 mg g$^{-1}$ was reported using agricultural waste-derived biochar, while[1–4] achieved 324.2 mg g$^{-1}$ with activated carbon from rice husks. The source of this data is the study itself albeit more details about the study are necessary for further interpretation. Additionally, our system achieved 73% TDS, 50% COD, and 99% conductivity reductions for real textile wastewater. Comparable works utilizing waste-derived adsorbents have reported lower treatment efficiencies despite higher operating costs. Parvin *et al.* removed only 67% TDS and 35% COD using orange peel-based biochar-activated carbon.[29] Compared to the percolation infiltration procedure, this study found that iron oxide-rich sand treats organic contamination better.[3] Different functional groups (–OH, Fe–O, Al–O, Si–O, and Ti–O) and oxides ($Fe_2O_3$, $TiO_2$, $SiO_2$, *etc.*) in the black sand column are detected using FTIR spectroscopy XRD and XRF. Therefore, the authors suggest a mechanism based on the

Table 3 Analysis of raw and treated industrial wastewater using black sand assisted with and without UV lamp

| Parameter | Inlet stream | Output stream using UV | Output stream without UV | Removal efficiency% with UV | Removal efficiency% without UV |
|---|---|---|---|---|---|
| COD (ppm) | 1000 | 496 | 850 | 50.40 | 15 |
| TDS (ppm) | 950 | 250 | 700 | 73.68 | 26.32 |
| TSS (ppm) | 890 | 500 | 750 | 43.82 | 15.73 |
| Conductivity (μS) | 950 | 13.6 | 30 | 98.57 | 96.84 |
| pH | 8.6 | 8.6 | 8.6 | — | — |

interactions between functional groups on black sand and organic substances, specifically –OH and sand-surface ion exchanges that may maintain organic substances. The adsorption process was electrostatic contact because sand has a zero-point charge.[3]

### ANOVA results

The ANOVA test was conducted at a 95% confidence level ($\alpha = 0.05$) to determine the statistical significance of the variables. The results are shown in Tables 1–5.

The low $p$-values (<0.05) indicate that changes in all the tested parameters significantly impacted the MB removal by applying the black sand filtration system. Bed height showed the least influence among the variables. This analysis informs the selection of optimum operational conditions.

The percent removal of MB increased as the bed height increased from 10 cm to 20 cm. At a greater bed height, the adsorbate has more contact area with activated carbon, allowing for more adsorption sites to be utilized before the effluent is discharged. This trend agrees with previous reports, which observed an improvement in adsorbate removal by increasing column bed depth due to the greater availability of adsorption sites.

The percentage removal of MB increased as the contact time increased from 30 to 60 minutes for a given bed height and flow rate. A longer contact time allows the adsorbate to interact more with activated carbon interior surfaces and micropores, increasing the probability of successful adsorption. This behaviour aligns with adsorption kinetics models, which show that adsorption rates are initially rapid before slowing down as equilibrium is approached.

The percentage removal of MB decreased as the initial MB concentration increased from 25 ppm to 100 ppm; at higher concentrations, the available adsorption sites became more saturated. This agrees with the literature, noting that saturation of favourable sites at high concentrations lowers overall removal efficiency. Percentage removal decreased as the flow rate increased from 1 mL $min^{-1}$ to 3 mL $min^{-1}$. Faster flow rates reduce contact and residence time between the adsorbate and activated carbon, limiting adsorbate diffusion into carbon micropores and surface adsorption. Similar trends have been widely reported in column adsorption studies.

### Proposed adsorption mechanism

Based on the characterization and performance analysis, the methylene blue (MB) adsorption mechanism likely involves a combination of interactions with the black sand's surface functional groups and photocatalytic degradation.

FTIR analysis revealed the presence of various functional groups on the black sand surface, such as silanols (Si–OH), aluminols (Al–OH), and iron oxyhydroxides (Fe–O–H), which could actively participate in MB adsorption. The XRD results confirmed the presence of iron oxides, such as magnetite and hematite, which are known for their excellent adsorption properties. The iron oxides present could adsorb MB through surface complexation between the nitrogen/oxygen atoms in MB and $Fe^{3+}$ cations on the iron oxide surface.

The hydroxyl groups of iron oxides/oxyhydroxides and silica could form hydrogen bonds with the nitrogen/oxygen atoms in the MB dye molecules. Additionally, π–π interactions and electrostatic attractions between the positively charged nitrogen atoms in MB and negatively charged sites on the black sand surface also contribute to the enhanced adsorption capacity. Thus, the synergistic effect of various interactions facilitated the efficient removal of MB onto the black sand surface.[31] Additionally, electron–hole pairs are generated on the photocatalyst surface upon UV irradiation. The photoexcited electrons reduce oxygen to superoxide radicals, while the holes oxidize hydroxide ions and water to hydroxyl radicals ($OH^{\bullet}$).[32] These reactive oxygen species then degrade the MB molecules *via* substitution, dehydrogenation, and ring-opening reactions.[33]

### Adsorption isotherm and kinetic models

The adsorption isotherm describes the interaction between adsorbate molecules and the adsorbent surface at equilibrium. This study applied the Langmuir and Freundlich isotherm models to describe the experimental adsorption data.

The Langmuir isotherm model assumes monolayer adsorption onto a homogeneous surface with a finite number of identical sites. The linear form of the Langmuir isotherm is given as follows:

$$1/q_e = 1/q_m K_L/C_e + 1/q_m, \quad (7)$$

where $q_e$ is the amount of dye adsorbed per unit mass of adsorbent (mg $g^{-1}$), $C_e$ is the equilibrium dye concentration in solution (ppm), $q_m$ is the maximum monolayer adsorption capacity (mg $g^{-1}$), and $K_L$ is the Langmuir constant related to the affinity of binding sites (L $mg^{-1}$).

The Freundlich isotherm model assumes heterogeneous surface energies with a non-uniform distribution of heat of

Table 4 ANOVA analysis of experimental parameters

| Parameter | Sum of squares | df | Mean square | $F$ value | $p$-Value | Significance |
|---|---|---|---|---|---|---|
| pH | 0.0879 | 2 | 0.0439 | 18.29 | 0.002 | Yes |
| Bed height | 0.0326 | 2 | 0.0163 | 6.76 | 0.022 | Yes |
| Flow rate | 0.0755 | 2 | 0.0377 | 15.63 | 0.004 | Yes |
| Contact time | 0.0544 | 2 | 0.0272 | 11.28 | 0.012 | Yes |
| Error | 0.0144 | 6 | 0.0024 | — | — | — |
| Total | 0.2648 | 14 | — | — | — | — |

adsorption over the heterogeneous surface. The linear form is expressed as follows:

$$\ln q_e = \ln K_F + (1/n) \ln C_e, \quad (8)$$

where $K_F$ is the Freundlich constant, indicating the adsorption capacity, and $1/n$ is the adsorption intensity.

The kinetic data were analyzed using the pseudo-first order, pseudo-second order, and Bohart–Adams models to understand the adsorption mechanism and rate-determining steps. As detailed earlier, the Bohart–Adams model fitted best with the experimental dynamic adsorption data ($R^2 = 0.97$), indicating that surface diffusion was the rate-limiting step in the continuous adsorption process.

### Proposed photocatalytic degradation mechanism

A possible mechanism for the UV-activated photocatalytic degradation of methylene blue dye by black sand is proposed here.

The iron and titanium oxides in the black sand particles act as photocatalysts. When irradiated by UV light energy equal to or greater than the bandgap energies, electrons ($e^-$) in the valence band are excited to the conduction band, creating electron–hole ($h^+$) pairs. The strong oxidizing potential of hole sites ($h^+$) on the photocatalyst surface leads to the generation of hydroxyl radicals ($^{\bullet}OH$) *via* oxidation of adsorbed $H_2O$ or $OH^-$ ions. Electrons ($e^-$) in the conduction band can also reduce dissolved $O_2$ to superoxide radicals ($O_2^{-\bullet}$). These highly reactive $^{\bullet}OH$ and $O_2^{-\bullet}$ radicals then initiate the breakdown of adsorbed methylene blue dye molecules into smaller intermediates through processes such as hydrolysis, oxidation, and substitution reactions. Upon continued radical attack, the intermediates may further degrade to simpler molecules, such as $CO_2$, $H_2O$, $NO_3^-$, chloride, and sulfate ions. Eventually, full mineralization of the organic contaminant occurs. The regenerated photocatalyst is then available to adsorb and degrade fresh dye pollutants from water under continued UV irradiation.

The following reactions summarize the proposed mechanisms, as illustrated in eqn (9)–(11).

Photogeneration of charge carriers:

$$TiO_2 \text{ or } Fe_2O_3 \text{ (from black sand)} + h\nu \rightarrow e^- \text{ (conduction band)} + h^+ \text{ (valence band)}. \quad (9)$$

Formation of hydroxyl radicals:

$$h^+ + H_2O \rightarrow OH^{\bullet} + H^+ \quad (10)$$

MB degradation:

$$MB + OH^{\bullet} \rightarrow \text{intermediates} \rightarrow CO_2 + H_2O. \quad (11)$$

### Comparison with other studies

The literature extensively describes the photocatalytic destruction of organic contaminants. When solar light has photon energy greater than the photocatalyst's band gap energy, it is absorbed to form electrons and holes. A redox reaction occurs on the photocatalyst surface as electron–hole pairs migrate. Many of these holes and electron pairs recombine to release light and heat. The photocatalyst's holes in the valence band attack the methylene blue dye and mix with water to form hydroxyl radicals that strongly oxidize it. The unrecombined electrons are excited to the conduction band. More energized electrons attack oxygen to create. Superoxide anion radicals breakdown methylene blue dye into carbon dioxide, water, and other non-toxic compounds using photocatalysts and light. Lighting and photocatalyst type affect photocatalysis efficiency.[34]

Methylene blue dyes degrade well with metal oxide photocatalysts—zirconium oxide nanoparticles photocatalyzed 89.11% methylene blue degradation under sun irradiation. Sn-doped MgO performed better than un-doped MgO as a photocatalyst for methylene blue degradation. The photocatalyst's metal dopant content affected performance. Using nickel oxide–cobalt oxide heterojunction systems, MB dye was destroyed over 85% in contaminated water. Carbon-based compounds are commonly layered with heterojunction chalcogenides to improve separation after use. The carbon nanotubes with $CuBi_2O_4/AgBiO_3$ heterojunction degraded 97.94% after 1 h of visible light irradiation.[34] Photocatalyst graphitic carbon nitride has a bandgap energy of 2.7 eV, making it unique among carbon-based materials. This means that it supports the other photocatalyst and accelerates the MB dye photocatalytic breakdown. Using $\alpha$-$Fe_2O_3$/g-$C_3N_4$ as a photocatalyst resulted in a 2.6-fold increase in photocatalytic efficiency for MB degradation under UV light compared to using plain $\alpha$-$Fe_2O_3$. These materials, called doped photocatalysts, often improve photodegradation performance several times. Examples include Sn-doped MgO, $\alpha$-$Fe_2O_3$/g-$C_3N_4$, $CuBi_2O_4/AgBiO_3$, $TiO_2$/g-$C_3N_4$, and Ag/$WO_3$. This is because the doped photocatalysts lower the band gap, for example, from 2.6 eV to 2.1 eV for Ag/$WO_3$. A comparison of photocatalyst materials, synthesis methods, operating conditions, and methylene blue removal efficiency (R.R) has been reported in the literature compared to this work (Table 5).[34] The present work using black sand assisted with a UV lamp resulted in a notable maximum adsorption capacity ($q_{max}$) of 562.43 mg $g^{-1}$ for removing MB dye. This is comparable to other low-cost adsorbents reported in the literature, such as river sand, which achieved a $q_{max}$ of 81.5 mg $g^{-1}$ for MB removal.[15] The coupling of adsorption using black sand with photocatalytic degradation using UV irradiation enhances MB removal compared to adsorption alone. A previous study by ref. 35 reported 86.2% removal of MB using a $TiO_2$/g-$C_3N_4$@Ag photocatalyst under 3 h UV irradiation. The present work achieved 90% removal of 50 ppm MB using black sand with a UV lamp at optimal conditions of pH 10 and a flow rate of 53.33 mL $min^{-1}$. The synergistic effect of adsorption by black sand and photocatalysis by UV irradiation likely contributed to the higher removal efficiency compared to photocatalysis alone.

Overall, the combined adsorption-photocatalysis approach using locally available black sand as a low-cost adsorbent with

Table 5 Photocatalytic degradation of MB in the literature

| Compound and synthetic technique | Photocatalytic conditions | Efficiency | Ref. |
|---|---|---|---|
| CuO (green synthesis) | 3 h irradiation; 10 mL (20 ppm) of dyes; 10 ppm of CuO NPs | 92.00% | 36 |
| Bi/CdS/$TiO_2$ (SILAR method) | Presence of Cr(VI); 3 h | 100.00% | 37 |
| $ZnAl_2O_4$ (microwave-combustion) | Simulated sunlight; 160 min | 85.70% | 38 |
| Multi-walled CNTs/$Fe_3O_4$ (one-step co-precipitation) | Time of 60 min; 40 mg of photocatalyst; 100 mL MB; pH 11, temperature of 50 °C | 98.49% | 39 |
| Zinc oxide/zeolite (two-step hydrothermal) | 34% w/w composite; $t = 60$ min; pH = 7; $C_{MB} = 100$ ppm | 76.00% | 40 |
| Ag/$SnO_2$ (simple co-precipitation) | 25 mL/15 mg; 2.5 mol $L^{-1}$ MB; 2 h | 97.63% | 41 |
| Ag/$WO_3$ (deposition–precipitation synthesis technique) | Visible light illumination in 120 min at 1 g $L^{-1}$ catalyst dosage | ~80% | 42 |
| Carbonaceous nitrogen-doped zinc oxide/reduced graphene oxide (coupling strategy) | Simulated solar light; 1 h; 10 ppm,; initial pH of 8; catalyst dosage of 0.4 g $L^{-1}$ | 98.90% | 43 |
| rGO–$NiWO_4$/$Bi_2S_3$ (green sol–gel) | 40 min; pH of 4; 10 ppm | 57.71% | 44 |
| $TiO_2$/g-$C_3N_4$@Ag (thermal polycondensation/sol–gel/chemical reduction) | MB, 20 ppm, UV-A illumination for 3 h | 86.2% | 45 |
| rGO/Gd/$BiVO_4$ (hydrothermal and ultra-sonication) | Visible-light irradiation; 100 min | 97.00% | 46 |
| Multi-walled CNTs/ZnO/chitosan ternary nanocomposite (interfacial engineering technique) | 20 min; UV light | 98.76% | 47 |
| α-$Fe_3O_4$ (thermal decomposition) | Visible light; 70 min; pH 9 | 70.00% | 48 |
| Polyamide/silver/reduced graphene (deposition) | 20 min; Ag/rGO (5 : 100 mg) | 98.00% | 49 |
| α-$F_{e2}O_3$/$LaFeO_3$/g-$C_3N_4$/$Ti_3C_2$ (deposition)- | Presence of Cr(VI); 91.30% in 40 min | 91.30% | 50 |
| CdS/Cd-metal–organic framework (*in situ* sulfurization) | 10 mg photocatalyst; 100 min | 91.90% | 51 |

UV lamp irradiation shows promise as an eco-friendly and effective technique for removing dye pollutants from wastewater. The performance is comparable to or better than other reported photocatalytic systems in the literature.[13,35]

## General discussion

The adsorption of methylene blue onto the black sand is well described by applying Langmuir and Freundlich isotherm models, indicating monolayer coverage and heterogeneous binding sites. Photocatalytic degradation follows the principles of semiconductor physics, where optical excitation of the iron and titanium oxide bandgap generates electron–hole pairs that enable redox reactions. The rapid pseudo-second-order kinetics align with the literature on dye adsorption mechanisms.[52] Compared to $TiO_2$, the multiphasic composition of the black sand lowers the bandgap energy to 2.1 eV, enhancing visible light absorption for photocatalysis.[53] X-ray spectroscopy confirms the presence of active photocatalytic phases, such as iron titanates. The kinetics outperform many single-component photocatalysts.[34]

The maximum adsorption capacity of 562.43 mg $g^{-1}$ exceeds recent reports on agricultural waste biochar (350 mg $g^{-1}$) and MOF hybrids (482 mg $g^{-1}$) for methylene blue uptake.[51] This demonstrates the potential of locally sourced black sand to replace costly activated carbon, which has shown superior performance primarily in batch studies. The 93% dye removal at pH 10 matches the literature on cationic dye adsorption favoured under alkaline conditions.[54] The improved performance with increased bed height and contact time adheres to established trends in fixed-bed adsorption.[55] The findings showcase black sand's viability for economical and eco-friendly water treatment.[1,2,4,5,11,13,21,27–29,46–49]

Column adsorption experiments provide practical insights into scalable systems, overcoming the limitations of batch characterizations. The flow rate, pH, and initial dye concentration span industrially relevant ranges. The models effectively describe the breakthrough curves across conditions ($R^2 > 0.95$), validating the Thomas and Yoon–Nelson model applicability. The material characterizations mutually reinforce the proposed adsorption and photocatalytic mechanisms.

## Policy and commercialization outlook

This work demonstrates a sustainable wastewater treatment method utilizing indigenous resources with the potential for affordable dye removal under 3 USD per kg of adsorbent. Adoption could aid textile and tannery facilities in meeting effluent regulations. The high treatment capacity, regeneration potential, and simple column configuration showcase commercial viability. Transitioning the bench-scale column to on-site pilots and, eventually, industrial-scale systems would

provide an eco-friendly and economically feasible solution for organic wastewater remediation.

## Conclusion

This study set out to develop an innovative wastewater treatment method using locally sourced black sand, assisted by UV irradiation, to remove methylene blue dye through combined adsorption and photocatalytic degradation. Systematic experimentation with a continuous fixed-bed column achieved up to 90% dye removal and a maximum adsorption capacity of 562.43 mg $g^{-1}$ under optimal conditions. Mathematical models effectively predicted the breakthrough curves. For real textile wastewater, the black sand filtration + UV system showed significantly higher COD, TDS, TSS, and conductivity reductions than filtration alone. Characterization revealed the predominance of iron and titanium oxides in the sand, which promoted dye adsorption and photocatalysis upon UV activation. The technology demonstrates a sustainable, scalable, and affordable alternative to activated carbon filtration for removing recalcitrant organic pollutants from industrial effluents. Further research should explore system performance for additional contaminants and wastewater types. With sufficient treatment efficiency demonstrated at the pilot scale, commercialization would provide textile and related industries with an economical and eco-friendly wastewater treatment solution.

## Author contributions

Conceptualization, R. W., M. F. and A. E. S.; methodology, R. W., M. F., R. M., and A. E. S.; software, R. M. and A. E. S.; validation, R. M.; formal analysis R. W., R. M., and A. E. S.; investigation, A. E. S.; resources, A. E. S.; data curation, R. W., M. F., and A. E. S.; writing—original draft preparation, R. M., M. F. and A. E. S.; writing—review and editing, R. W., R. M., A. E. S. and M. F.; visualization, A. E. S.; supervision, R. W., M. F., and A. E. S. All authors have read and agreed to the published version of the manuscript.

## Conflicts of interest

The authors confirm this article has no conflict of interest.

## Acknowledgements

The authors would like to express their appreciation to the University of Zagazig, Faculty of Engineering, Environmental Engineering Laboratory.

## References

1 M. Kebir, *et al.*, Water Cleaning by a Continuous Fixed-Bed Column for Cr (VI) Eco-Adsorption with Green Adsorbent-Based Biomass An Experimental Modeling Study, *Processes*, 2023, **11**, 363.
2 H. Kumari, *et al.*, A Review on Photocatalysis Used For Wastewater Treatment: Dye Degradation, *Water, Air, Soil Pollut.*, 2023, **234**(6), 349.
3 R. E. Haouti, *et al.*, Removal of heavy metals and organic pollutants by a sand rich in iron oxide, *Euro-Mediterranean J. Environ. Integr.*, 2018, **3**, 1–11.
4 A. S. Elkholy, M. S. Yahia, M. A. Elnwawy, H. A. Gomaa and A. S. Elzaref, Synthesis of activated carbon composited with Egyptian black sand for enhanced adsorption performance toward methylene blue dye, *Sci. Rep.*, 2023, **13**, 4209.
5 T. Nguyen, *et al.*, A Fixed-Bed Column Study for Removal of Organic Dyes from Aqueous Solution by Pre-Treated Durian Peel Waste, *Indones. J. Chem.*, 2019, **19**, 486, DOI: **10.22146/ijc.39712**.
6 A. Halim, K. K. Han and M. Hanafiah, Removal of methylene blue from dye wastewater using river sand by adsorption, *Nat., Environ. Pollut. Technol.*, 2015, **14**, 89–94.
7 M. Barros, P. Arroyo and E. Silva, General aspects of aqueous sorption process in fixed beds, ed. H. Nakajima, 2013, pp. 361–386.
8 A.-A. M. Abdel-Karim, S. M. Zaid, M. I. Moustafa and M. G. Barakat, Mineralogy, chemistry and radioactivity of the heavy minerals in the black sands, along the northern coast of Egypt, *J. Afr. Earth Sci.*, 2016, **123**, 10–20.
9 M. Z. Khedr, *et al.*, Genesis and evaluation of heavy minerals in black sands: A case study from the southern Eastern Desert of Egypt, *Geochemistry*, 2023, **83**, 125945.
10 R. Farouq, Coupling Adsorption-Photocatalytic Degradation of Methylene Blue and Maxilon Red, *J. Fluoresc.*, 2022, **32**, 1381–1388, DOI: **10.1007/s10895-022-02934-1**.
11 M. Kebir, *et al.*, Water Cleaning by a Continuous Fixed-Bed Column for Cr(VI) Eco-Adsorption with Green Adsorbent-Based Biomass: An Experimental Modeling Study, *Processes*, 2023, **11**, 363.
12 A. López-Vásquez, A. Suárez-Escobar and F. E. López-Suárez, Black Sand-Based Photocatalyst for Hydrogen Production from EDTA Solutions Under UV-Vis Irradiation, *Top. Catal.*, 2020, **63**, 1325–1335, DOI: **10.1007/s11244-020-01286-z**.
13 A. El Shahawy, I. A. Ahmed, R. Wagdy, A. H. Ragab and N. H. Shalaby, Phragmites australis (Reed) as an Efficient, Eco-Friendly Adsorbent for Brackish Water Pre-Treatment in Reverse Osmosis: A Kinetic Study, *Molecules*, 2021, **26**, 6016.
14 APHA, *Standard Methods for the Examination of Water and Wastewater*, APHA, 1985.
15 A. A. Halim, K. K. Han and M. M. Hanafiah, Removal of methylene blue from dye wastewater using river sand by adsorption, *Nat., Environ. Pollut. Technol.*, 2015, **14**, 89.
16 O. Allahdin, *et al.*, Adsorption capacity of iron oxyhydroxide-coated brick for cationic metals and nature of ion–surface interactions, *Appl. Clay Sci.*, 2014, **90**, 141–149, DOI: **10.1016/j.clay.2014.01.008**.
17 A. López-Vásquez, A. Suárez-Escobar and F. López-Suárez, Black Sand-Based Photocatalyst for Hydrogen Production from EDTA Solutions Under UV-Vis Irradiation, *Top. Catal.*, 2020, **63**, 1325–1335.

18 N. Mahdadi, S. Chihi, H. Bouguettaia, S. Beddiaf and M. L. Mechri, Chromatic Classification of Ouargla (Algeria) Dunes Sand: Determination of Main Compositions and Color Causes, by Using XRD, FTIR and XRF, *Silicon*, 2017, **9**, 211–221, DOI: 10.1007/s12633-016-9432-x.

19 R. Morsi and R. El-Sayed, Nanostructured mesoporous silica: Influence of the preparation conditions on the physical-surface properties for efficient organic dye uptake, *R. Soc. Open Sci.*, 2018, **5**, 172021, DOI: 10.1098/rsos.172021.

20 S. N. Lawandy, R. Sayed, B. K. Saleh and S. Halim, Utilization of Nano-Black Sand as filler in Styrene Butadiene Rubber composites, *Egypt. J. Chem.*, 2019, **63**(6), 2051–2062.

21 G. Anbalagan, A. R. Prabakaran and S. Gunasekaran, Spectroscopic characterization of Indian standard sand, *J. Appl. Spectrosc.*, 2010, **77**, 86–94, DOI: 10.1007/s10812-010-9297-5.

22 K. J. Lagos, *et al.*, Data on phase and chemical compositions of black sands from "El Ostional" beach situated in Mompiche, Ecuador, 2020, **32**, 106214.

23 M. W. Ansari, A. Nadeem, M. W. Ansari and A. Nadeem, *Anatomy of the Orbit*, 2016, pp. 1–10.

24 R. E. Morsi and R. S. Mohamed, Nanostructured mesoporous silica: influence of the preparation conditions on the physical-surface properties for efficient organic dye uptake, *R. Soc. Open Sci.*, 2018, **5**(3), 172021.

25 R. E. Haouti, *et al.*, Removal of heavy metals and organic pollutants by a sand rich in iron oxide, *Euro-Mediterranean J. Environ. Integr.*, 2018, **3**, 17, DOI: 10.1007/s41207-018-0058-9.

26 A Thesis Presented to the Faculty of Engineering University of Santo Tomas In Partial Fulfillment of the Requirements for the Degree of Bachelor of Science in Chemical Engineering: (R. E. Piquero, Design, fabrication and initial evaluation of an up-flow fixed-bed adsorption column for lead ($Pb^{2+}$) using Carica papaya seeds, 2005).

27 M. A. S. D. Barros, P. A. Arroyo and E. A. Silva, General aspects of aqueous sorption process in fixed beds, *Mass Transfer–Advances in Sustainable Energy and Environment Oriented Numerical Modeling*, ed. H. Nakajima, 2013, pp. 361–386.

28 O. Kopsidas, *Scale-Up of Adsorption in Fixed-Bed Column Systems*, 2016.

29 G. S. Bohart and E. Q. Adams, Behavior of charcoal towards chlorine, *J. Chem. Soc.*, 1920, **42**(7), 523–529.

30 N. Begum, N. Khuzaima, F. F. Ching, M. F. Bari and S. Rezan, Characterization of Langkawi Black Sand for the Recovery of Titanium, *Key Eng. Mater.*, 2016, **709**, 70–73, DOI: 10.4028/www.scientific.net/KEM.709.70.

31 A. Sharma, *et al.*, Carbon nano-structures and functionalized associates: Adsorptive detoxification of organic and inorganic water pollutants, *Inorg. Chem. Commun.*, 2022, **141**, 109579.

32 N. Nasuha, S. Ismail and B. Hameed, Activated electric arc furnace slag as an effective and reusable Fenton-like catalyst for the photodegradation of methylene blue and acid blue 29, *J. Environ. Manage.*, 2017, **196**, 323–329.

33 W. A. Aboutaleb, I. M. Nassar, R. M. Mahmoud, A. Marey and R. A. El-Salamony, Black sand as a cost-effective catalyst for methylene blue photo-remediation under visible light, *Discov. Sustain.*, 2023, **4**, 39.

34 P. O. Oladoye, T. O. Ajiboye, E. O. Omotola and O. J. Oyewola, Methylene blue dye: Toxicity and potential elimination technology from wastewater, *Results Eng.*, 2022, **16**, 100678, DOI: 10.1016/j.rineng.2022.100678.

35 R. Farouq, Coupling Adsorption-Photocatalytic Degradation of Methylene Blue and Maxilon Red, *J. Fluoresc.*, 2022, **32**, 1381–1388, DOI: 10.1007/s10895-022-02934-1.

36 H. D. Shelke, *et al.*, Multifunctional $Cu_2SnS_3$ nanoparticles with enhanced photocatalytic dye degradation and antibacterial activity, *Materials*, 2022, **15**, 3126.

37 Q. Wang, *et al.*, Construction of Bi-assisted modified CdS/$TiO_2$ nanotube arrays with ternary S-scheme heterojunction for photocatalytic wastewater treatment and hydrogen production, *Fuel*, 2022, **322**, 124163.

38 A. Talati and M. Haghighi, Hard-templating design of mesoporous $ZnAl_2O_4$ *via in situ* microwave combustion method as an efficient solar-light-responsive nanophotocatalyst for photo-decomposition of organic dyes from aqueous solution, *J. Photochem. Photobiol., A*, 2022, **430**, 113955.

39 S. Hussain, *et al.*, A facile low-cost scheme for highly photoactive $Fe_3O_4$-MWCNTs nanocomposite material for degradation of methylene blue, *Alexandria Eng. J.*, 2022, **61**, 9107–9117.

40 H. Tehubijuluw, R. Subagyo, Y. Kusumawati and D. Prasetyoko, The impregnation of ZnO onto ZSM-5 derived from red mud for photocatalytic degradation of methylene blue, *Sustainable Environ. Res.*, 2022, **32**, 1–12.

41 H. A. Shittu, *et al.*, Effect of low-doping concentration on silver-doped $SnO_2$ and its photocatalytic applications, *Biointerface Res. Appl. Chem.*, 2023, **13**, 165.

42 M. Maha, *et al.*, Visible Light Photocatalytic Activity of Ag/$WO_3$ Nanoparticles and its Antibacterial Activity Under Ambient Light and in The Dark, *Results Eng.*, 2022, **33**, 100313.

43 M. M. Kaid, *et al.*, Effective photocatalytic degradation of organic dyes using ZNC/rGO nanocomposite photocatalyst derived from ZIF-8/rGO thermolysis for water treatment, *J. Photochem. Photobiol., A*, 2022, **430**, 114001.

44 H. Liaquat, *et al.*, Citric acid-capped $NiWO_4/Bi_2S_3$ and rGO-doped $NiWO_4/Bi_2S_3$ nanoarchitectures for photocatalytic decontamination of emerging pollutants from the aqueous environment, *Environ. Res.*, 2022, **212**, 113276.

45 I. Ibrahim, *et al.*, Silver decorated $TiO_2$/g-$C_3N_4$ bifunctional nanocomposites for photocatalytic elimination of water pollutants under UV and artificial solar light, *Results Eng.*, 2022, **14**, 100470.

46 S. Bashir, *et al.*, Gd-doped $BiVO_4$ microstructure and its composite with a flat carbonaceous matrix to boost photocatalytic performance, *J. Alloys Compd.*, 2022, **913**, 165214.

47 M. Malekkiani, A. Heshmati Jannat Magham, F. Ravari and M. Dadmehr, Facile fabrication of ternary MWCNTs/ZnO/

Chitosan nanocomposite for enhanced photocatalytic degradation of methylene blue and antibacterial activity, *Sci. Rep.*, 2022, **12**, 5927.

48 A. Dehno Khalaji, Spherical $\alpha$-$Fe_2O_3$ Nanoparticles: Synthesis and Characterization and Its Photocatalytic Degradation of Methyl Orange and Methylene Blue, *Phys. Chem. Res.*, 2022, **10**, 473–483.

49 S. Elbakry, *et al.*, Photocatalytic degradation of organic compounds by TFC membranes functionalized with Ag/rGO nanocomposites, *J. Photochem. Photobiol., A*, 2022, **430**, 113957.

50 W. Zhang, *In situ* synthesis of $\alpha$-$Fe_2O_3$/$LaFeO_3$ modified with g-$C_3N_4$ and $Ti_3C_2$ for construction of multiple Z-scheme/Schottky heterojunctions as an efficient visible-light photocatalyst for Cr (VI) reduction and organic pollutants removal, *J. Alloys Compd.*, 2022, **913**, 165217.

51 C. Jing, et al., *In situ* constructing visible light CdS/Cd-MOF photocatalyst with enhanced photodegradation of methylene blue, *Particuology*, 2022, **69**, 111–122.

52 M. Benjelloun, Y. Miyah, G. A. Evrendilek, F. Zerrouq and S. Lairini, Recent advances in adsorption kinetic models: their application to dye types, *Arabian J. Chem.*, 2021, **14**, 103031.

53 X. Wu, *et al.*, Facile *in situ* construction of highly dispersed nano zero-valent iron modified black $TiO_2$ Z-scheme recyclable heterojunction with highly efficient visible-light-driven photocatalytic activity, *Appl. Catal., B*, 2022, **310**, 121325.

54 S. Farch, *et al.*, Application of Walnut Shell Biowaste as an Inexpensive Adsorbent for Methylene Blue Dye: Isotherms, Kinetics, Thermodynamics, and Modeling, *Separations*, 2023, **10**, 60.

55 H. B. Quesada, *et al.*, Caffeine removal by chitosan/activated carbon composite beads: Adsorption in tap water and synthetic hospital wastewater, *Chem. Eng. Res. Des.*, 2022, **184**, 1–12.